

# Coulomb explosion dynamics of $N_2$ in intense laser field by mass-resolved momentum imaging<sup>1</sup>

Akiyoshi Hishikawa<sup>a,b</sup>, Atsushi Iwamae<sup>a,b</sup>, Kennosuke Hoshina<sup>a,b</sup>, Mitsuhiko Kono<sup>a,b</sup>, Kaoru Yamanouchi<sup>a,b,\*</sup>

<sup>a</sup> Department of Chemistry, School of Science, The University of Tokyo, 7-3-1 Hongo, Bunkyo-ku, Tokyo 113-0033, Japan  
<sup>b</sup> Japan Science and Technology, Kawaguchi Center bldg., 4-1-8 Hon-cho, Kawaguchi, Saitama 332-0012, Japan

Received 4 November 1997

## Abstract

The Coulomb explosion reactions of  $N_2$ ,  $N_2^{(p+q)+} \rightarrow N^{p+} + N^{q+}$ , caused by the irradiation of intense laser light ( $0.73\text{--}6.9 \text{ PW/cm}^2$ ) were investigated by high-resolution time-of-flight (TOF) mass spectroscopy and by the mass-resolved two-dimensional momentum imaging (MRMI) method. Six explosion pathways  $(p, q) = (1, 1), (1, 2), (1, 3), (2, 2), (2, 3)$  and  $(3, 3)$  in addition to  $(0, 1), (0, 2)$  dissociation pathways were identified, whose assignments were securely performed both from the momentum matching between the fragment pair and their correlation with the laser-field intensity dependence. The MRMI method, which visualizes the radial and angular momentum distributions of mass-selected fragment ions on a two-dimensional momentum plane, was used to correlate ion fragments produced after the Coulomb explosion. By examining theoretically synthesized MRMI maps, it was found that the momentum distributions of the fragment ions in a wide momentum range can be extracted by the MRMI technique. The relative yields of the explosion pathways at six different laser-field intensities were evaluated from the three-dimensional integration of the MRMI maps, and the intensity dependence of the formation of singly and multiply charged parent  $N_2^{(p+q)+}$  ions prior to the fragmentation was derived. © 1998 Elsevier Science B.V. All rights reserved.

## 1. Introduction

In an intense laser field of several tens of petawatt/cm<sup>2</sup> ( $1 \text{ PW/cm}^2 = 10^{15} \text{ W/cm}^2$ ), the magnitude of the electric field generated by the laser light pulse becomes as large as that of the Coulombic field felt by an electron in an atom. When such a strong oscillatory field interacts with molecules, an interaction between a molecule and the laser-light

field cannot be treated in a perturbative manner, because it should be included as one of the dominant terms of a total Hamiltonian [1,2]. Recent advances in high-power, ultrashort-pulse laser technology has enabled us to investigate the behavior of molecules in such intense laser fields. For example, the Coulomb explosion phenomena [3–36] and the alignment and manipulation of the molecular beam in the intense laser fields [37,38] have been studied both experimentally and theoretically.

It has been known that molecules are formed in their highly multiply charged state in the duration of the ultrashort laser pulse, and subsequently, the bond

\* Corresponding author. E-mail: kaoru@chem.s.u-tokyo.ac.jp

<sup>1</sup> Dedicated to Professor Ikuzo Tanaka on the occasion of his 70th birthday.

fission process occurs to generate multiply charged photofragments having very high kinetic energy. This phenomenon called the Coulomb explosion in an intense laser field was first reported by Codling and Frasiniski [3] in 1987, and has become one of the fascinating research targets in these several years. It may be worthy to remark here that the Coulomb explosion phenomena were also observed in the beam-foil [39], single photon impact [40,41] and electron impact [42,43] experiments. It was also reported that the Coulomb explosion of molecules occurs after the collision of multiply-charged atomic ions with target molecules [44–46].

For the molecular Coulomb explosion in an intense laser field, Frasiniski et al. [4] introduced a covariance mapping technique in order to correlate multiply charged fragments produced after the explosion reactions. For the Coulomb explosion of  $N_2$  molecules, they demonstrated that fragment ions with a certain charge number are produced from parent molecules with different charge numbers; for example,  $N^+$  can be formed from both  $N_2^{2+}$  and  $N_2^{3+}$  from the explosion reactions,  $N_2^{2+} \rightarrow N^+ + N^+$  and  $N_2^{3+} \rightarrow N^+ + N^{2+}$ . For polyatomic molecules, it has also been shown that the covariance mapping technique [5,8] and its variation called the double correlation mapping technique introduced by Cornaggia and Normand [20–22] are useful to correlate multiply-charged photofragments produced after the Coulomb explosion.

It has also been reported that molecules are aligned along the laser polarization direction. The angular distribution of the ejected ion fragments after the Coulomb explosion was investigated for  $H_2$  [27],  $I_2$  [28], and  $CO$  [7,19] by measuring the ion signal intensities at different laser polarization angles with respect to the detection axis. Hatherly et al. [7] and Normand et al. [19] reported the narrower angular distribution of  $CO$  for the atomic ion fragments with a larger charge number. Similar techniques were adopted recently for the investigation of the Coulomb explosion of  $CCl_4$ ,  $CHCl_3$ , and  $CH_2Cl_2$  [30].

Recently, we introduced a new method called mass-resolved momentum imaging (MRMI) to investigate the angular distribution of the ion fragments produced after Coulomb explosion reactions [24]. It has been demonstrated that the high resolving power in the mass spectral measurements is crucial for

identifying the correlations among the fragment ions. The MRMI maps for  $N_2$  at  $3.5 \text{ PW/cm}^2$  exhibited the clear angular distributions of the fragments on the momentum plane. The different-charge channels having the same momentum distributions are correlated with each other using both the kinetic energy release and the angular distribution projected on the MRMI map, and consequently, the  $(p, q)$  pathways of the Coulomb explosion,  $N_2^{(p+q)+} \rightarrow N^{p+} + N^{q+}$ , were identified. The MRMI method has also been applied to the Coulomb explosion of  $SO_2$  in the intense laser field ( $5.4 \text{ PW/cm}^2$ ), from which the fission pathways were investigated. As has been shown in our recent report, this MRMI method based on the high-resolution time-of-flight (TOF) mass spectroscopy afforded the clearest imaging picture of the angular and radial momentum distributions of the fragment ions produced after the Coulomb explosion. The MRMI approach is promising to investigate the Coulomb explosion pathways, which is complementary with the previous procedures such as the covariance mapping [5] and the double correlation mapping [20], in which statistical events of the simultaneous formation of the ion fragments were accumulated to correlate these fragment ions.

The Coulomb explosion of  $N_2$  in an intense laser field was first observed by Frasiniski et al. [3] in 1987 using the intense picosecond laser at 600 nm, and the kinetic energy releases of the  $N^+$ ,  $N^{2+}$ , and  $N^{3+}$  fragment ions in the (1, 1), (1, 2), (2, 2), and (2, 3) pathways were reported. In 1989, Boyer et al. [23] analyzed their TOF spectra, and found that the charge-asymmetric fragmentation pathways such as (0, 2) and (1, 3) were abundant at 248 nm. From the covariance mapping technique, Frasiniski et al. [4] identified the weak asymmetric (1, 3) pathway as well as the prevalent charge-symmetric (2, 2) and (3, 3) at 600 nm. In 1991, Cornaggia et al. [17] measured TOF mass spectra at 615 nm, and reported that  $N^{3+}$  with the release energy of 9.5 eV originated from the asymmetric (1, 3) channel. However, in 1991, Codling et al. [9] reported that no assignable signal was found for the (1, 3) pathway in their covariance maps at 305 and 600 nm. In 1993, Stankiewicz et al. [13] was not able to identify the (1, 3) pathway either in their covariance maps obtained at 305 and 248 nm, though the other pathways such as (1, 1), (1, 2), (2, 2), (2, 3), and (3, 3), were

identified. The history described here tells us that the consensus has not been reached regarding the existence of the asymmetric (1, 3) pathway.

In the present study, we investigate the Coulomb explosion of  $N_2$  by varying the laser-field intensity in order to derive the secure assignments of the Coulomb explosion pathways in an intense laser field and their laser-field intensity dependence. Previously, we were able to identify the asymmetric (1,3) explosion pathway from the high-resolution TOF spectrum. These assignments are confirmed by the intensity dependence of the relative yields of the explosion pathways including the (1, 3) pathway, as well as by the information of the radial and angular distribution contained in the MRMI map. On the basis of the present assignments, the relative abundances of the ( $p, q$ ) fission pathways are derived as a function of the laser-field intensity for the first time through the three-dimensional integration of the MRMI maps. Furthermore, a method to construct theoretical MRMI maps is introduced, in which a finite ion-detector size is taken into account. From the simulation of the MRMI maps, it is explained how the dynamical information is encoded in the two-dimensional MRMI map. The procedure to read the information about the ultrafast Coulomb explosion dynamics from the MRMI is also discussed.

## 2. Experimental

Some of the details of our experimental set up have also been reported in Ref. [24]. Femtosecond laser pulses at 795 nm with a typical pulse duration of 52 fs were generated by a mode-locked Ti-sapphire laser (Spectra-Physics Tsunami) which was pumped by a frequency-doubled output of a diode-laser-pumped Nd:YVO<sub>4</sub> laser (Spectra-Physics Millennia). The output of the Tsunami was introduced to a regenerative amplifier system (BM-Industry Alpha 10B/S), in which the two sequential bow-tie amplifier stages were used to amplify the output of a regenerative amplifier, to obtain high-power low-repetition-rate (10 Hz) short-pulsed laser light. After the pulse compressor, the duration of the amplified laser pulse  $\tau_L$  was 100 fs, measured by an auto-correlator (MC2 Femtoscope), and the total energy reached as high as 50 mJ/pulse.

The light beam was focused by a quartz lens ( $f = 152$  mm at 795 nm) onto a pulsed molecular beam between the extraction parallel repeller plates of a linear time-of-flight (TOF) mass spectrometer (Jordan Linear-TOF) with a flight length of 1400 mm. The singly and multiply charged atomic and molecular ions produced after Coulomb explosion were extracted by the repeller field through a meshed aperture (10 mm $\phi$ ), and after the acceleration, they were detected by a microchannel-plate (MCP) detector placed at the end of flight tube. The diameter of the aperture is sufficiently large so that the ion-acceptance angle was determined by the size of the MCP detector. The extraction and acceleration voltages were 372 and 3811 V, respectively. The spacing between the repeller plates was measured carefully with a cylinder gauge to be 12.45 mm, which yields the extraction electric field of 298.7 V/cm. Typical mass resolution of  $m/\Delta m \approx 620$  achieved under these experimental conditions was much higher than the previous studies for the molecular Coulomb explosion and enabled us to resolve the ion species produced after different multiply-charged states of a parent diatomic molecule. The TOF mass spectra were recorded and averaged over  $1 \times 10^3$  shots by a digital oscilloscope (LeCroy 9370) with a 1 GHz sampling rate. In deriving the MRMI map, a zero-order half-wave plate was introduced after the compressor stage of the Alpha-10 system in order to rotate a laser polarization plane with respect to the detection axis of the TOF mass spectrometer.

By assuming a Gaussian spatial profile, the spot size of the laser beam at the focal point was estimated to be  $2w_0 = 13$   $\mu\text{m}$  in diameter. This means that the laser-field intensity defined as  $E_L/(\pi w_0^2 \tau_L)$  becomes 7 PW/cm<sup>2</sup> at the molecular beam when the output of the regenerative amplifier system  $E_L$  is 1 mJ/pulse. The main chamber and the TOF tube were differentially pumped by two turbo molecular pumps (Balzers/Pfeiffer Vacuum TMU 520 (520 l/s) for the main chamber and TMU 260 (210 l/s) for the TOF tube). Each of the two turbo molecular pumps was backed up by an oil-free scroll pump (Anest-Iwata ISP-250; 250 l/min) to achieve oil-free vacuum conditions. The nitrogen gas was introduced into the main chamber through a pulsed valve. When the pulsed valve was not operated, the background pressure in the main chamber was  $\sim 1.2 \times 10^{-8}$

Torr and that in the TOF tube was  $\sim 1.0 \times 10^{-8}$  Torr. After the collimation by a skimmer, a molecular effusive beam was introduced into the laser–molecule interaction region located 120 mm downstream from the nozzle orifice (0.5 mm $\phi$ ). During the experiment, the pressure in the main chamber was kept sufficiently low ( $< 1 \times 10^{-7}$  Torr) in order to avoid the space charge effect [16].

### 3. Momentum-scaled TOF spectra

#### 3.1. Assignments of Coulomb explosion pathways

When the laser polarization direction was set parallel to the TOF detection axis, all the mass peaks of nitrogen atomic ions,  $N^+$ ,  $N^{2+}$ , and  $N^{3+}$ , in our TOF mass spectrum at 3.5 PW/cm $^2$  split to form a doublet as seen in the lower trace of Fig. 1. These doublets mean that the produced atomic ions travelled first in the forward and backward directions, causing a flight time difference between the two

types of fragments due to the extraction field of the TOF mass spectrometer, i.e., the forward fragments were accelerated further and the backward fragments were decelerated first and changed the direction to forward and then accelerated. The total kinetic energy release,  $U$ , for the fragmentation pathway,  $N_2^{(p+q)+} \rightarrow N^{p+} + N^{q+}$ , was obtained from the time separation of the doublet peaks in the TOF spectrum for the  $N^{q+}$  channel as

$$U = (\Delta t)^2 (qF)^2 / m, \quad (1)$$

where  $\Delta t$  represents a half of the time difference between the split mass peaks,  $F$  the static electric field for ion extraction, and  $q$  and  $m$  the charge and mass of the fragment, respectively. The initial momentum,  $mv_0$ , imposed on the fragment due to the Coulomb explosion can be written as

$$mv_0 = qF\Delta t, \quad (2)$$

with the initial velocity of the fragment  $v_0$  along the flight axis.

From the fine structure in the doublet peaks observed in the high-resolution TOF spectrum, the

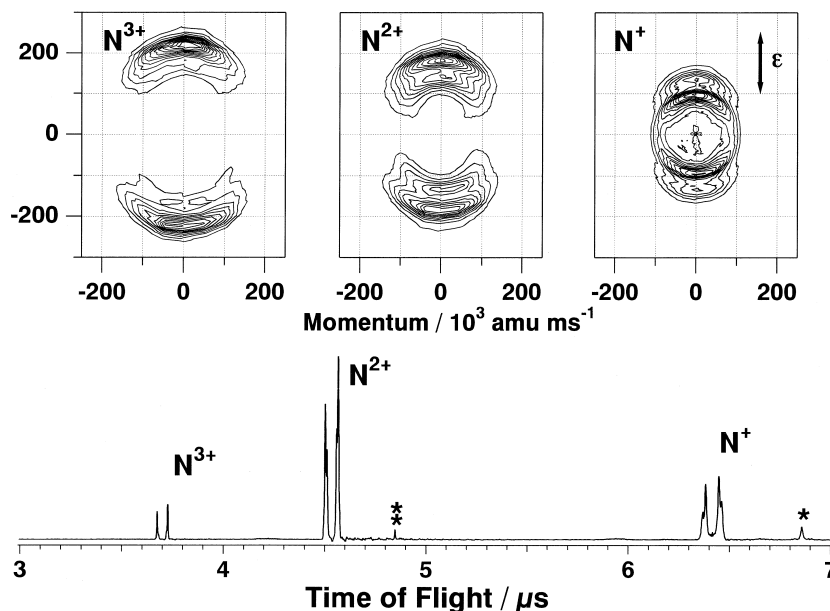


Fig. 1. Lower trace: The TOF ion-mass spectrum of  $N_2$  at the laser-field intensity of 3.5 PW/cm $^2$  recorded with the laser polarization direction parallel to the detection axis of the TOF mass spectrometer. The doublet peaks are identified for the ion species,  $N^{3+}$ ,  $N^{2+}$ , and  $N^+$ . The small peaks marked with one asterisk and two asterisks are assigned to the  $O^+$  and  $O^{2+}$  signals, respectively, from  $H_2O$ . Upper panels: The MRMI maps of  $N_2$  at 3.5 PW/cm $^2$  for the  $N^{3+}$  (left),  $N^{2+}$  (middle), and  $N^+$  (right) channels. The scale of the intensity contour of each picture is normalized by the maximum intensity. The vertical arrow indicates the direction of the laser polarization vector. It should be noted that the angular distribution becomes narrower for higher charged fragments.

explosion fragment pathways can be identified. In Fig. 2, the  $N^+$ ,  $N^{2+}$ , and  $N^{3+}$  channel regions in the TOF spectra measured at three different laser-field intensities (2.1, 3.5, and 6.9 PW/cm<sup>2</sup>) are expanded with an abscissa scale linear to the momentum imposed on the atomic ion fragments. In these momentum-scaled TOF spectra, all the three channels exhibited a partially split double-peak structure with a small shoulder on the larger momentum side, indicating the existence of at least three Coulomb explosion pathways for each of the three ion channels.

When the Coulomb explosion occurs starting from multiply charged parent ions;  $N_2^{(p+q)+} \rightarrow N^{p+} + N^{q+}$ , equal amounts of the momentum are imposed on both of the ionic fragments. Therefore, by comparing the  $N^{2+}$  channel with the other  $N^+$  and  $N^{3+}$  channels in Fig. 2, the counterpart atomic fragments

associated with the three components in the  $N^{2+}$  channel can be easily identified. The lowest momentum peak ( $\sim 140 \times 10^3$  amu m/s) among the three components in the  $N^{2+}$  channel is formed with the  $N^+$  channel, and the highest momentum peak ( $\sim 220 \times 10^3$  amu m/s) is formed with the  $N^{3+}$  channel. Consequently, the center peak in the three components ( $\sim 180 \times 10^3$  amu m/s) forms two  $N^{2+}$  fragments. It can be concluded that the three pathways, (1,2), (2,2), and (2,3), produce the  $N^{2+}$  fragment ion with different momenta.

In a similar manner, the (1,1) pathway is identified in the  $N^+$  channel, in addition to the (1,2) pathway. On the lower momentum side of these two pathways, a weak tail extending towards the lower momentum region can be identified. This tail part is assigned to the (0,1) pathway, having much smaller

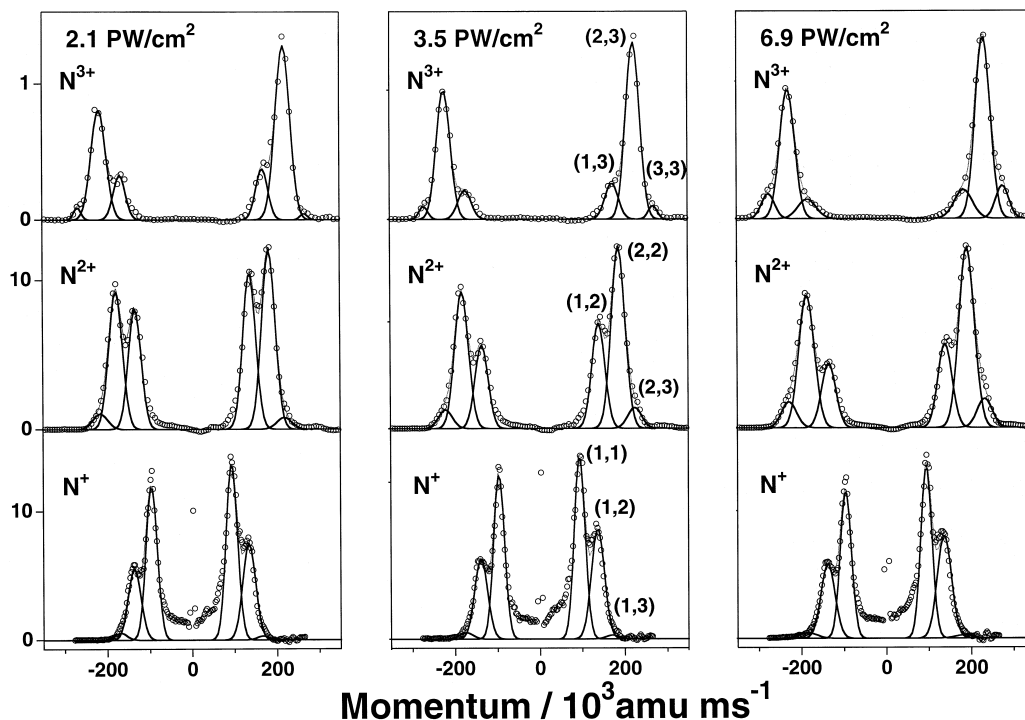


Fig. 2. Variation of experimental momentum-scaled TOF spectra (open circle) at the laser-field intensities of 2.1, 3.5, and 6.9 PW/cm<sup>2</sup> for different channels:  $N^{3+}$  (top),  $N^{2+}$  (middle), and  $N^+$  (bottom). The laser-field intensity increases from the left to the right. In these momentum-scaled TOF spectra, both the forward and backward peaks exhibit a partially-split double-peak structure with a small shoulder on the larger momentum side in all three channels. The assignments of the Coulomb explosion pathway ( $p, q$ ) was straightforward on the basis of the momentum matching. The least-squares fit was performed by assuming a Gaussian profile (solid curve) for each component. In the least-squares fit, constraints were imposed so that a pathway commonly observed in the two different ion-fragment channels, such as (1,2), (1,3), and (2,3) pathways, has the same kinetic energy release and the same momentum distribution in those channels.

momentum release than the Coulomb explosion pathways. The sharp centered peak in the  $N^+$  channel is assigned to the doubly charged parent ion,  $N_2^{2+}$ , which has the same  $m/q$  as  $N^+$ . These assignments are consistent with the previous ones obtained by the TOF [16,17] and covariance [3,9,12,18] measurements.

In our momentum-scaled TOF spectra, thanks to the high resolving power, the (1,3) pathway, in which charges are distributed to the two fragment ions asymmetrically, was identified. This asymmetrical charge distribution is not explicable on the Thomas–Fermi–Dirac model [10], and may be regarded as an evidence of a charge localization [31,32]. As described later in Section 3.3, the  $(p, q)$  assignments of the peaks performed here were confirmed by the laser-field intensity dependence of the peak intensities in the momentum-scaled TOF spectra.

By assuming that a Gaussian profile in the momentum distribution of the atomic fragments the least-squares fit to the partially resolved structure of all the three  $N^+$ ,  $N^{2+}$ , and  $N^{3+}$  ion channels was performed. The absolute values of the released momentum defined as the centers of the Gaussian profiles were determined with high precision. In the least-squares fit, a constraint was imposed so that a pathway commonly observed in different fragment channels had the same kinetic energy release and the same momentum distribution in those channels. Such pathways are (1,2) in the  $N^+$  and  $N^{2+}$  channels, (1,3) in the  $N^+$  and  $N^{3+}$  channels, and (2,3) in the  $N^{2+}$  and  $N^{3+}$  channels.

If we assign a single Gaussian profile to represent the (0,1) pathway in the tail region of the  $N^+$  channel on its small momentum side, it could have a wide momentum distribution covering the (1,1) and (1,2) regions. However, since it is expected that the (0,1) pathway has lower kinetic energy release than the (1,1) and (1,2) pathways, its momentum distribution may not extend into the (1,1) and (1,2) regions. Therefore, a single Gaussian profile is not appropriate to represent the momentum distribution of this weak (0,1) pathway. This broad momentum distribution for the (0,1) pathway may represent that the singly charged parent  $N_2^+$  ions are prepared in the energy region where the dissociation occurs with various fragmentation pathways having a wide range of the kinetic energy release.

Table 1

The total kinetic energies<sup>a</sup> (eV) released after the Coulomb explosion of  $N_2$  in the intense laser field<sup>b</sup>

Laser-field intensity (PW cm <sup>-2</sup> )	2.1	3.5	6.9
$N_2^{2+} \rightarrow N^+ + N^+$	6.66(7)	6.73(4)	6.71(2)
$N_2^{3+} \rightarrow N^+ + N^{2+}$	13.6(1)	14.08(6)	13.95(2)
$N_2^{4+} \rightarrow N^+ + N^{3+}$	21(2)	22.3(9)	25.2(7)
$N_2^{4+} \rightarrow N^{2+} + N^{2+}$	24.1(2)	25.23(6)	26.37(3)
$N_2^{5+} \rightarrow N^{2+} + N^{3+}$	35(1)	36.7(3)	39.3(1)
$N_2^{6+} \rightarrow N^{3+} + N^{3+}$	50(10)	54(3)	56.3(4)

<sup>a</sup>Determined from the least-squares fit to the momentum-scaled TOF spectra in Fig. 2.

<sup>b</sup>The laser-field intensity (PW cm<sup>-2</sup>) is defined as  $E_L / (\pi w_0^2 \tau_L)$  (see text).

In consequence, only the (1,1), (1,2), and (1,3) pathways were considered in the least-squares fit of the  $N^+$  channel, and the momentum data smaller than  $70 \times 10^3$  amu m/s were not included in the fit. Similarly, in order to reduce the influence of the (0,2) pathway in the tail region of the  $N^{2+}$  channel on its small momentum side, the momentum data of the  $N^{2+}$  channel smaller than  $110 \times 10^3$  amu m/s were not included in the fit. The least-squares fit to the observed profiles were performed with only small residuals as shown in Fig. 2 for the three different laser-field intensities. The momentum values for the six pathways, (1,1), (1,2), (1,3), (2,2), (2,3), and (3,3), were determined with high precision, and the corresponding released kinetic energies are listed in Table 1. It can be found that there is a weak dependence of the released kinetic energy on the laser-field intensity; as the laser-field intensity increases, these values tend to increase. However, the magnitude of the shifts is comparable with the uncertainties associated with the determined released kinetic energies.

The observed width of the momentum distribution of the atomic fragments has a contribution from: (1) the distribution of a momentum transferred after the Coulomb explosion; (2) the initial momentum distribution of the parent molecules at room temperature; and (3) a limited velocity resolution determined by the diameter of the MCP detector. The contribution from (3) will be discussed in Section 4.2. Our successful fit of the momentum distributions of the fragment ion channels described above indicates that the Gaussian profiles are appropriate to represent the mixture of these three contributions.

As shown in Fig. 2, the relative contributions of the  $(p, q)$  channels have a clear dependence on the laser-field intensity. For example, when the  $N^{2+}$  channel data recorded at three different laser-field intensities are compared, the peak intensity of the (2,2) pathway relative to that of the (1,2) pathway increases clearly as the laser-field intensity increases. This variation means that the abundance of the higher charged parent ion,  $N_2^{4+}$ , relative to the lower charged parent ion,  $N_2^{3+}$ , increases as the laser-field intensity increases. It can be said that this laser-field intensity dependence of the peak height in the momentum-scaled TOF represents that of the formation of the multiply charged parent ions. The quantitative analysis of the laser-field intensity dependence will be described in Section 3.3.

### 3.2. Intensity scaling of momentum-scaled TOF spectra

It should be noted that the intensity scale along the ordinate of the momentum-scaled TOF spectra in Fig. 2 is calibrated with respect to the charge number of the fragment. When the TOF mass spectrum represented as a function of the flight time is converted to the momentum distribution, the scale along the abscissa is multiplied by the charge number,  $q$ , of the ion fragment, according to Eq. (2). Therefore, in order to compare the relative yields of the fragments representing the different explosion pathways shown in Fig. 2, the observed signal intensity along the ordinate in the TOF spectrum is divided by the charge number. In Fig. 2, the intensity along the ordinate represents the scaled intensity.

Even after such scaling, it was found that the peak represented as (1,2) in the  $N^+$  channel and the (1,2) peak in the  $N^{2+}$  channel had different intensities. The total amount of the  $N^+$  ions produced from the (1,2) pathway should be equal to that of the  $N^{2+}$  ions from the same pathway. Therefore, the difference in the intensities of these peaks can be ascribed to that in the detection efficiency of the ionic fragments with a different charge number. The correction factor to account for the difference in the detection efficiency can be determined by the ratio of the peak area of the (1,2) pathway of the  $N^+$  channel,  $\sigma(N^+)$ , and that of the  $N^{2+}$  channel,  $\sigma(N^{2+})$ . The peak areas were calculated from the deconvoluted Gauss-

ian profiles, which were optimized by the least-squares fit to the partially resolved peaks in the momentum-scaled TOF spectra. From the comparison of the two peak areas, the scaling factor,  $\sigma(N^{2+})/\sigma(N^+)$ , of the  $N^{2+}$  channel with respect to the  $N^+$  channel was determined to be  $\sigma(N^{2+})/\sigma(N^+) = 1.50(10)$  as an averaged value at 3.5, 6.9, and 10.4 PW/cm<sup>2</sup> (Fig. 2).

In a similar manner, the scaling factor of  $\sigma(N^{3+})/\sigma(N^{2+}) = 1.24(16)$  was obtained from the (2,3) pathway, which is commonly observed in the  $N^{2+}$  and  $N^{3+}$  channels. Since  $\sigma(N^{3+})/\sigma(N^+) = \sigma(N^{3+})/\sigma(N^{2+}) \times \sigma(N^{2+})/\sigma(N^+)$  holds,  $\sigma(N^{3+})/\sigma(N^+) = 1.86(26)$  was determined. The similar factors were obtained for the fragment ion channels of the Coulomb explosion processes of NO [25].

### 3.3. Laser-field intensity dependence of the Coulomb explosion pathways

By using the determined areas of the deconvoluted Gaussian profiles in the momentum-scaled TOF spectra measured at the six different laser-field intensities (0.73, 1.0, 1.4, 2.1, 3.5, and 6.9 PW/cm<sup>2</sup>), the intensity dependences of the relative abundances of the seven Coulomb explosion pathways are plotted as shown in Fig. 3. As clearly shown in Fig. 3d, the  $N^+$  and  $N^{2+}$  channels of the (1,2) pathway exhibited almost the same laser-field intensity dependence. A similar correlation was observed in Fig. 3b for the  $N^{2+}$  and  $N^{3+}$  channels of the (2,3) pathway. These agreements of the intensity dependence for the  $N^{p+}$  and  $N^{q+}$  channels for the  $(p, q)$  pathway securely confirmed the assignments of the explosion pathways performed in Section 3.1 on the basis of the momentum matching in the momentum-scaled TOF spectra in Fig. 2. In addition to the  $(p, q)$  pathways, the center peak in the  $N^+$  channel representing the  $N_2^{2+}$  parent ion was also fitted using the Gaussian profile to discuss the relative abundance of the Coulomb explosion pathways. Furthermore, the contribution of the (0,1) pathway, exhibiting the broad distribution in the momentum-scaled TOF spectra in the  $N^+$  channel, was predicted by subtracting the optimized Gaussian profiles of the  $N_2^{2+}$  pathway and of the (1,1), (1,2), and (1,3) pathways from the observed momentum-scaled TOF spectrum for the  $N^+$  channel.

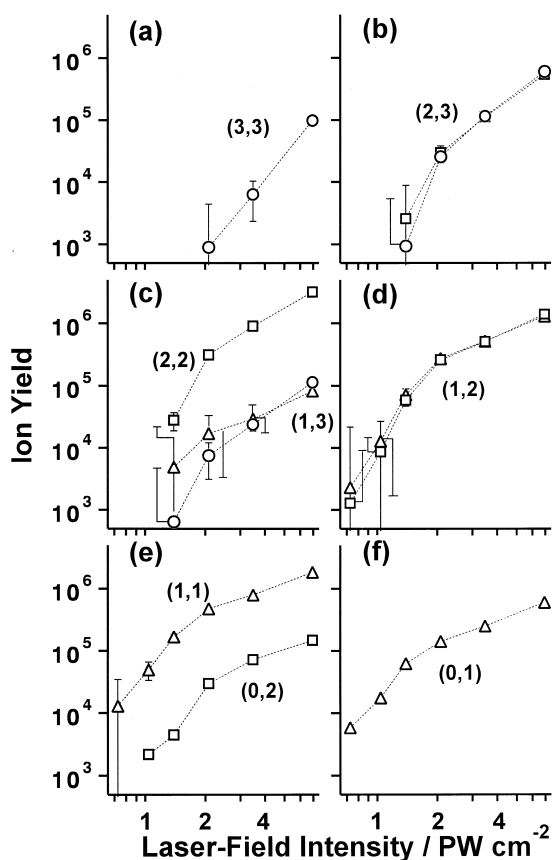


Fig. 3. The laser-field intensity dependence of the fragment ion yields obtained after the Coulomb explosion of  $N_2$  in an intense laser field. The ion yields were derived from the area of the Gaussian distributions determined by the least-squares fit to the experimental momentum-scaled TOF spectra. The detection efficiencies for  $N^{2+}$  and  $N^{3+}$  ions were calibrated to the  $N^+$  ion (see text). The fragment ions are classified by the change state of the parent  $N_2$  ions: (a)  $N^{3+}$  from the (3,3) pathway, (b)  $N^{3+}$  ( $\circ$ ) and  $N^{2+}$  ( $\square$ ) from the (2,3) pathway, (c)  $N^{2+}$  ( $\square$ ) from the (2,2) pathway, and  $N^{3+}$  ( $\circ$ ) and  $N^+$  ( $\triangle$ ) from the (1,3) pathway, (d)  $N^{2+}$  ( $\square$ ) and  $N^+$  ( $\triangle$ ) from the (1,2) pathway, (e)  $N^+$  ( $\triangle$ ) from the (1,1) pathway, and (f)  $N^+$  ( $\triangle$ ) from the (0,1) pathway. The uncertainties of fit were also presented for all the pathways except the (0,1) pathway. The errors for the (0,1) pathway were estimated to be within the size of the open circle. The laser-field dependence of the fragment ion yield confirmed the assignment of the explosion pathways proposed from the momentum matching.

In the case of the  $N^+$  and  $N^{3+}$  channels of the (1,3) pathway, the slope for the  $N^+$  channel is relatively shallower than the  $N^{3+}$  channel in the low

laser-field intensity region as shown in Fig. 3c. However, considering the  $N^+$  channel of the (1,3) pathway exhibits relatively large uncertainties due to its very small peak height, the laser-field intensity dependences of these two channels are in agreement with each other. It is interesting to note that the  $N^{3+}$  intensity for the (1,3) pathway exhibits almost the same dependence as the  $N^{2+}$  intensity for the (2,2) pathway in Fig. 3c. This coincidence indicates that the  $N^{2+}$  from the (2,2) pathway and  $N^+$  and  $N^{3+}$  from the (1,3) pathway are produced from the same charged state of the parent ions, i.e.  $N_2^{4+}$ , and that the branching ratio to produce the (1,3) and (2,2) pathways is not influenced sensitively by the laser-field intensity.

In a similar manner as the (0,1) pathway, the contribution of the (0,2) pathway was derived from the momentum-scaled TOF spectra for the  $N^{2+}$  channel in the small momentum region. The laser-field intensity dependence of the (0,2) pathway is plotted in Fig. 3e in comparison with the (1,1) pathway. The variation of the relative yield of the (0,2) pathway is in a good agreement with that of the (1,1) pathway, which supports the assignment of the (0,2) pathway to the weak and broad distribution in the  $N^{2+}$  channel.

## 4. Information contained in MRMI maps

### 4.1. Construction of MRMI maps from observed momentum-scaled TOF spectra

The MRMI maps for the Coulomb explosion of  $N_2$  were obtained by rotating the laser polarization in a stepwise manner. The half-wave plate was rotated manually with an angle interval of  $6^\circ$ , which corresponds with a polarization angle interval of  $12^\circ$ . In total  $\sim 15$  high-resolution TOF spectra were taken to construct an MRMI map. The MRMI patterns were constructed using all the data covering the  $180^\circ$  rotation. Information obtained from the angles between  $180^\circ$  and  $90^\circ$  should be the same as that from the angles between  $0^\circ$  and  $90^\circ$ , since a point symmetry is expected with respect to the origin of the two-dimensional momentum plane. The degree of asymmetry in the observed MRMI pattern with re-

spect to the line connecting the  $0^\circ$  and  $180^\circ$  positions, was used as diagnostics of the variation of the experimental conditions during the repetitive TOF data acquisition.

As shown in Fig. 4, the MRMI map is constructed by the contours connecting smoothly the same intensity level of the momentum-scaled TOF spectra observed at the different laser polarization angles,  $\alpha$ , with respect to the detection axis. In the upper panels of Fig. 1, the contour plots of the MRMI pictures for the  $N^+$ ,  $N^{2+}$ , and  $N^{3+}$  channels are displayed on a two-dimensional momentum plane. The shape of the cross-section along the vertical and horizontal axes in the imaging pictures corresponds with the mass-split patterns obtained when the laser polarization direction is parallel and perpendicular, respectively, to the TOF detection axis.

As clearly seen in the crescent-shaped domains in the three maps, the momentum of charged atomic fragments increases as the charge number of the fragment increases, and the angle spanned by the arc along the crescent-shaped distribution tends to become smaller. The increase of the momentum reflects the fact that the larger kinetic energies are released after the Coulomb explosion when the charge

number of the parent  $N_2^{(p+q)+}$  ion becomes larger. The decrease of the angle spanned by the arc reflects the fact that the extent of the alignment of an N–N molecular axis along the laser polarization becomes larger for the higher charged parent ions. This alignment effect will be described quantitatively in Section 4.2.

In the  $N^+$  channel, outside the clear crescent-shaped area, the less pronounced crescent can be seen. When we compare this imaging figure with the mass-pattern in the  $N^+$  channel in Fig. 2, the assignment of these areas is straightforward. The inner and outer crescent-shaped regions correspond with the (1,1) and (1,2) pathways. This kind of inner and outer crescent structure can also be seen in the MRMI picture of the  $N^{2+}$  channel. When we compare MRMI patterns of the  $N^+$  and  $N^{2+}$  channels in Fig. 1 expressed with the same momentum scale, the area of the outer crescent in the  $N^+$  channel almost overlap with the inner crescent in the  $N^{2+}$  channel. Considering the discussion in Section 3.1, this coincidence means that the momentum distributions of the  $N^+$  and  $N^{2+}$  coincide with each other, and both of the distributions are assigned as the contribution from the (1,2) pathway. As has been demonstrated

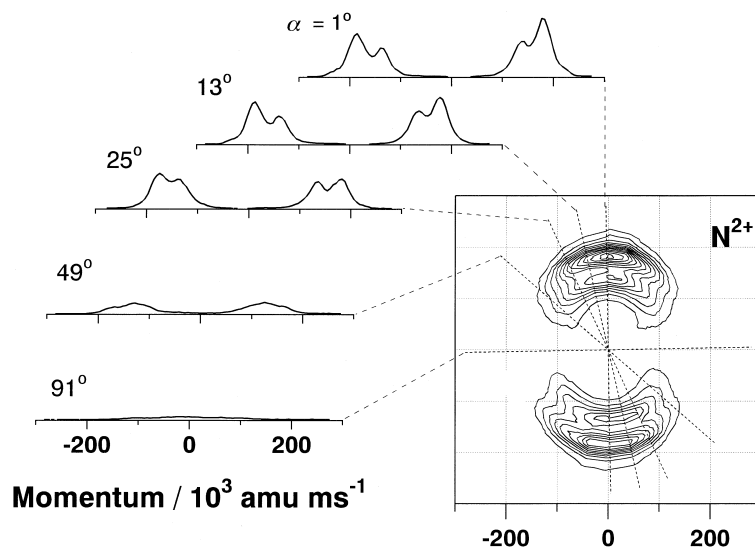


Fig. 4. Illustration of the MRMI procedure. An MRMI map is constructed from momentum-scaled TOF spectra measured with various angles  $\alpha$  between the laser polarization and the detector direction. The five experimental momentum-scaled TOF spectra of  $N^{2+}$  at  $3.5 \text{ PW/cm}^2$  with the angles of  $\alpha = 1^\circ, 13^\circ, 25^\circ, 49^\circ,$  and  $91^\circ$  are shown on the left-hand side of the MRMI map. Each of the momentum-scaled TOF spectra corresponds to the cross-section of the MRMI map at the angle  $\alpha$ . In total seventeen momentum-scaled TOF spectra were used to construct the contour MRMI map presented here.

here, one of the advantages of the MRMI method is that the correlation between multiply charged fragments is identified securely by comparing corresponding two-dimensional momentum areas having information of both momentum and angular distributions of the fragment ions.

#### 4.2. Theoretical synthesis of MRMI maps

When the detector size is infinitely small, an MRMI map represents the exact probability density distribution of the fragment ions on a momentum plane. However, since the area of the MCP detector is finite in practice, there is a certain limitation in the angular and the radial resolutions of the MRMI map. Therefore, it is necessary to know how the information of the Coulomb explosion dynamics is encoded in the MRMI map, and to establish a procedure to decode the dynamical information as precise as possible from an observed MRMI map.

If we define the angular resolution as an effective acceptance angle of the fragment ions by the detector, the angular resolution  $2\delta$ , which is a function of the detector size ( $d = 18 \text{ mm}\phi$ ) and the flight time  $T$  of the fragment ions of interest, is given as [24]:

$$\delta = \begin{cases} \sin^{-1} \frac{md}{2Tp_0} & (p_0 > md/2T) \\ \pi/2 & (p_0 \leq md/2T) \end{cases}, \quad (3)$$

where  $m$  represents the mass of the fragment ion. Though the effective acceptance angle tends to become smaller for the ion fragments with a larger momentum, it falls in  $\delta \sim 10^\circ$  for fast ions produced through the Coulomb explosion. This angular resolution is comparable with the angular interval ( $12^\circ$ ) of the polarization axis. For example, the acceptance angles for  $\text{N}^{2+}$  and  $\text{N}^{3+}$  fragments for the (2,3) pathway become  $\delta \sim 9^\circ$ , while that for  $\text{N}^+$  fragments for the (1,1) pathway is  $12^\circ$ .

If fragment ions have a constant momentum  $p_0$ , the radial momentum resolution originates from the time delay between the ions that reach the center of the detector and the ions that hit the edge of the detector. The momentum resolution  $\Delta p$  is expressed as:

$$\Delta p = p_0(1 - \cos \delta). \quad (4)$$

For the  $\text{N}^+$ ,  $\text{N}^{2+}$ , and  $\text{N}^{3+}$  fragments, the radial resolution on a momentum plane higher than  $\Delta p/p_0 = 5\%$  can be attained when the momentum exceeds  $63 \times 10^3$ ,  $90 \times 10^3$ , and  $109 \times 10^3$  amu m/s, respectively.

These results indicate that both the radial and angular resolutions on the momentum plane are sufficiently high for ions with large released momenta produced through a typical Coulomb explosion, so that the interpretation of the MRMI maps is rather straightforward. However, for ions with smaller momenta than  $\sim 70 \times 10^3$  amu m/s for  $\text{N}^{q+}$  ( $q = 1-3$ ) ions, the MRMI map would exhibit the momentum distributions deformed considerably from its original form by the finite resolution limited by the detector size. The extraction of the original momentum distribution function from the MRMI maps would require simultaneous consideration of the angular and the radial resolutions on the momentum plane as expressed in Eqs. (2) and (3).

Since the MRMI maps are constructed from the TOF spectra in the momentum scale obtained with different polarization directions with respect to the detector, it is necessary to understand first how the momentum-scaled TOF spectrum taken with a finite detector area is deformed from the original momentum distribution. The experimental momentum-scaled TOF spectrum can be considered as that obtained when an ideal momentum-scaled TOF spectrum obtained with an infinitely small detector area is convoluted with a certain instrumental function. Thus, in order to derive the detailed information about the original radial and angular distribution on the momentum plane, it is necessary to deconvolute the experimental momentum-scale TOF spectra.

To find the convolution function in momentum space, we assume that the momentum distribution function  $P(p, \beta)$  is separable into two components, i.e., the radial momentum distribution  $P(p)$  and angular momentum distribution  $P(\beta)$ , where the angle  $\beta$  is defined as the polar angle from the polarization direction as shown in Fig. 5. Furthermore, the ejected ions are assumed to have a single radial momentum,  $P(p) = \delta(p - p_0)$ , and the angular distribution,  $P(\beta)$ , axially symmetric with respect to the polarization vector  $\epsilon$  of the laser light. If the momentum-space fixed frame ( $X_p, Y_p, Z_p$ ) is introduced with the  $Z_p$  axis directed towards the

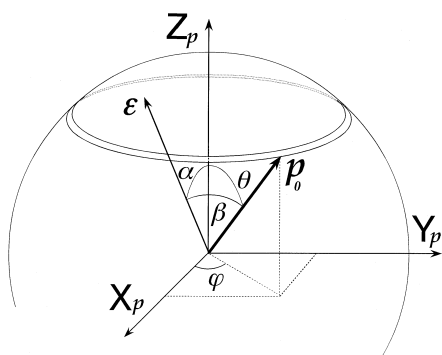


Fig. 5. Illustration of the coordinate system in the momentum space ( $X_p$ – $Y_p$ – $Z_p$ ) adopted in the present study. The  $Z_p$ -axis is directed towards the direction of the ion detector of the TOF mass spectrometer. The laser polarization vector  $\epsilon$ , which is located in the  $X_p$ – $Z_p$  plane, spans a polar angle  $\alpha$  with respect to the  $Z_p$  axis. The momentum vector  $p_0$ , along which the fragment ions which are ejected from the origin of the coordinate system, is expressed with the angular coordinates  $(\theta, \varphi)$ . The angle  $\beta$ , defined as the angle between the polarization vector  $\epsilon$  and the ion ejection vector  $p_0$ , can be expressed in terms of the three angle parameters,  $\alpha$ ,  $\theta$ , and  $\varphi$  as given in text.

detector (Fig. 5), the ion-ejection direction and the laser polarization vectors are expressed with the angular coordinates  $(\theta, \varphi)$  and  $(\alpha, 0)$ , respectively. By using these coordinates, the angle  $\beta$  can be expressed as

$$\beta = \cos^{-1}(\sin \alpha \sin \theta \cos \varphi + \cos \alpha \cos \theta). \quad (5)$$

Therefore, the angular intensity  $dI$  of the ions ejected in a polar angle between  $\theta$  and  $\theta + d\theta$  is given as:

$$\begin{aligned} dI &= \int_0^{2\pi} [P(\beta) p_0^2 \sin \theta d\theta] d\varphi \\ &= p_0^2 \sin \theta d\theta \int_0^{2\pi} P(\beta) d\varphi. \end{aligned} \quad (6)$$

Since the component of the ion momentum along the detector direction is expressed as  $p_d = p_0 \cos \theta$ , the distribution density function,  $dI/dp_d$  is given as:

$$\frac{dI}{dp_d} = p_0 \int_0^{2\pi} P(\beta) d\varphi. \quad (7)$$

Therefore, a convolution function,  $g_\alpha(p_d, p_0)$ , corresponding to the TOF spectrum for the ions with a single momentum,  $p_0$ , is expressed as:

$$g_\alpha(p_d, p_0) = \begin{cases} p_0 \int_0^{2\pi} P(\beta) d\varphi & (p_0 - \Delta p \leq |p_d| \leq p_0) \\ 0 & (|p_d| \leq p_0 - \Delta p) \end{cases}. \quad (8)$$

In general, the TOF spectra in the momentum scale may be expressed as:

$$G_\alpha(p_d) = \int_0^\infty P(p_0) g_\alpha(p_d, p_0) dp_0, \quad (9)$$

which is applicable to any ion species irrespective of the magnitude of the released momentum  $p_0$ . Thus, when the momentum distribution function  $P(p_0)$  and the angular distribution function  $P(\beta)$  are provided, the TOF spectra in momentum space can be simulated for an arbitrary angle  $\alpha$  between the detector and the polarization direction by using Eq. (9).

Since an MRMI map is constructed from the momentum-scaled TOF spectra, the MRMI map can be simulated in a straightforward manner from the calculated momentum-scaled TOF spectra. A simulated MRMI map for the  $N^{3+}$  ion ejected through the (2, 3) pathway is shown in Fig. 6a, where  $P(p_0)$  is approximated by a Gaussian with the peak momentum  $p_0 = 223 \times 10^3$  amu m/s and the FWHM  $\Delta p_0 = 37.9 \times 10^3$  amu m/s. The angular distribution was approximated to be  $P(\beta) = \cos^k \beta$  and the experimental result for the (2, 3) pathway as shown in Fig. 1 was best reproduced with  $k = 7.5$ .

Previously, we reported  $k = 7.0(5)$  based on the experimental MRMI map of the  $N^{3+}$  ion produced through the (2, 3) pathway [24]. When the  $k$  value is estimated from the simulated MRMI map in a similar manner,  $k = 7.15(1)$  was obtained instead of  $k = 7.5$ . The reduction of the  $k$  value results from the broader angular distribution than the original one, which is attributed to the finite angular resolution, since the radial resolution is sufficiently high ( $\Delta p/p \approx 1\%$ ) in this momentum range. Therefore, the previously obtained parameter,  $k = 7.0(5)$ , can be corrected to be  $k = 7.4(5)$  by adding the corresponding shift in  $k$ ,  $\Delta k = 7.5 - 7.15 = 0.35$ , obtained here for the theoretical MRMI. This effect of the finite resolutions in the  $k$  value is less pronounced for the smaller  $k$  values in the large momentum range, because the widths of the original angular distributions along the coordinate  $\beta$  become sufficiently broader than the angular resolution  $\delta$ . Thus the angular distribution parameters  $k = 2.8(3)$  and  $6.0(5)$  reported previously for the (1, 1) and (2, 2) pathways, respectively, are expected to represent correctly the

original distribution within the estimated uncertainties.

Fig. 6b shows an MRMI map simulated for the same ionic species  $N^{3+}$  but with a small radial momentum distribution ( $p_0 = 22.3 \times 10^3$  amu m/s,  $\Delta p_0 = 3.79 \times 10^3$  amu m/s), which is scaled by 1/10 from the MRMI simulation presented in Fig. 6a. In this momentum range, the angular resolution  $2\delta$  is determined to be  $180^\circ$  from Eq. (3), which indicates that the  $N^{3+}$  ions ejected in any directions can reach the detector. However, as illustrated in Fig. 6b, even in such a momentum region, the MRMI map preserves the information of the radial and angular momentum distribution. Such anisotropic structures have been observed in the MRMI maps of  $SO^+$  in slow momentum region ( $< 50 \times 10^3$  amu m/s), which was produced through the Coulomb explosion of  $SO_2$  in an intense laser field [24].

### 5. Laser-field intensity dependence of the Coulomb explosion pathways

In Section 3.3, the laser-field intensity dependence of the Coulomb explosion pathways was dis-

cussed in terms of the area of the deconvoluted Gaussian profiles in the momentum-scaled TOF spectra. In order to compare quantitatively the relative yields of the fragment ions produced through the various explosion pathways, the difference in their angular distributions discussed in Section 4.2 should be taken into account.

An MRMI map,  $G_\alpha(p)$ , represents the density distribution of fragment ions on a momentum plane in the large momentum region. Therefore, the total yields of the fragment ions can be derived by integrating of the MRMI map along the angular (polar and azimuthal) and radial coordinates in the three-dimensional momentum space, where the  $z$ -axis in the momentum plane is located on the laser polarization axis.

In order to take into account the finite size of the ion detector of the TOF spectrometer, the integration was performed by the following procedures. First, the azimuthal integration factor  $A$  is introduced, which is a ratio of the azimuthally integrated area at a certain polar angle  $\alpha$  to the area spanned by the ion detector in the momentum space. Using the angle between the detector and the laser polarization direction,  $\alpha$ , and the acceptance angle of the detector,  $\delta$ ,

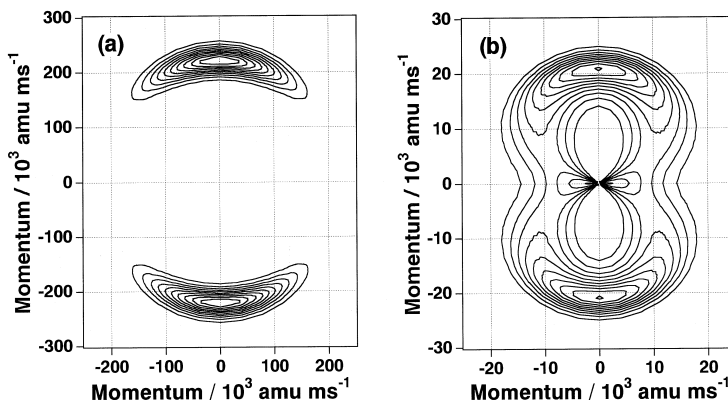


Fig. 6. The theoretically synthesized MRMI map for the  $N^{3+}$  ion, with the time of flight,  $T = 3.6 \mu\text{s}$ , and the detector size of  $d = 18 \text{ mm}\phi$ . (a) The simulated MRMI map for the (2,3) pathway: the radial momentum distribution is expressed as a Gaussian shape with the peak momentum,  $p_0 = 223 \times 10^3$  amu m/s, and the FWHM  $\Delta p_0 = 37.9 \times 10^3$  amu m/s, which were determined from the Gaussian fit to the momentum-scaled TOF spectrum as explained in Section 3.3. The angular distribution was approximated by  $P(\beta) = \cos^4 \beta$ , with  $\beta = 7.5$ . The simulated MRMI shows a clear crescent-shaped region, in good agreement with the experimental MRMI (Fig. 1). (b) The simulated MRMI map for the small momentum region below  $50 \times 10^3$  amu m/s. The radial momentum distribution is scaled by 1/10 from (a), i.e.,  $p_0 = 22.3 \times 10^3$  amu m/s and  $\Delta p_0 = 3.79 \times 10^3$  amu m/s. It can be noticed that the MRMI map carries the information of the original momentum distribution even when the acceptance angle for the detector becomes  $180^\circ$ .

Table 2

The relative abundances of the fragmentation pathways from  $N_2^{(p+q)+}$  produced in the intense laser field at six different intensities<sup>a</sup>

Laser-field intensity (PW cm <sup>-2</sup> )	0.73	1.0	1.4	2.1	3.5	6.9
$N_2^+ \rightarrow N + N^+$	0.43	0.35	0.29	0.19	0.16	0.13
$N_2^{2+} \rightarrow N + N^{2+}$	0.02	0.03	0.02	0.03	0.04	0.03
$N_2^{2+} \rightarrow N^+ + N^+$	0.45	0.47	0.37	0.30	0.24	0.19
$N_2^{3+} \rightarrow N^+ + N^{2+}$	0.10	0.15	0.22	0.27	0.25	0.23
$N_2^{4+} \rightarrow N^+ + N^{3+}$	– <sup>b</sup>	– <sup>b</sup>	0.05	0.05	0.05	0.05
$N_2^{4+} \rightarrow N^{2+} + N^{2+}$	– <sup>b</sup>	– <sup>b</sup>	0.04	0.14	0.20	0.25
$N_2^{5+} \rightarrow N^{2+} + N^{3+}$	– <sup>b</sup>	– <sup>b</sup>	0.01	0.02	0.05	0.09
$N_2^{6+} \rightarrow N^{3+} + N^{3+}$	– <sup>b</sup>	– <sup>b</sup>	0.00	0.00	0.01	0.03

<sup>a</sup>Defined as  $E_L/(\pi w_0^2 \tau_L)$  (see text).<sup>b</sup>Not identified.

as defined in Eq. (3) the integration factor  $A$  is expressed as

$$A(p, \alpha) = \begin{cases} 2 \sin \alpha \sin \delta / (1 - \cos \delta) & (\delta < \alpha) \\ [1 - \cos(\alpha + \delta)] / (1 - \cos \delta) & (\delta > \alpha) \end{cases} \quad (10)$$

By multiplying the factor,  $A(p, \alpha)$ , to the every point on the MRMI map, the integration along the azimuthal coordinate was performed.

The resultant MRMI map,  $\langle G_\alpha(p) \rangle = A(p, \alpha)G_\alpha(p)$ , obtained after the azimuthal integration, which is referred to as the azimuthally integrated MRMI map, was further processed to the two-dimensional radial and polar angle integrations. The yields of fragment ions in a specific pathway can be derived by integrating the corresponding region of the azimuthally integrated MRMI map along the radial and polar angle directions. For simplicity, the boundaries of the integration regions were approximated by constant-momentum circles on the azimuthally-integrated MRMI map. The radius of the momentum circle dividing the two explosion pathways was approximated by the momentum at the crossing point of the two deconvoluted Gaussian functions in the momentum-scaled TOF spectra. The total yields of the ions derived from the three-dimensional integrations of the MRMI map at the laser-field intensity of 3.5 PW/cm<sup>2</sup> (Fig. 1, upper panels) are listed in Table 2 for the seven explosion pathways.

The integrated ion yields at five different laser-field intensities other than 3.5 PW/cm<sup>2</sup> were derived in a following scheme: (1) the conversion factor from the area under the optimized Gaussian profile to the integrated ion yields was derived at 3.5 PW/cm<sup>2</sup> for each fragmentation pathway, and then

(2) the integrated ion yield for each of the five laser-field intensities was obtained by multiplying the determined conversion factor to the Gaussian area for each pathway in the momentum-scaled TOF spectra under the assumption that the conversion factors are independent of the laser intensity. The determined relative yields of the eight  $(p, q)$  pathways exhibited pronounced dependences on the laser-field intensity as shown in Table 2, reflecting the variation of the peak laser-field intensity at the focal point as well as that of the laser focal volume.

The relative abundances of the parent ions of  $N_2^{(p+q)+}$  prior to the fragmentation are plotted in Fig. 7 as a function of the laser-field intensity. The abundances for  $N_2^+$ ,  $N_2^{3+}$ ,  $N_2^{5+}$ , and  $N_2^{6+}$  were derived directly from the relative yields for the (0, 1), (1, 2), (2, 3) and (3, 3) pathways, respectively, while those for  $N_2^{2+}$  and  $N_2^{4+}$  were derived as the sum of

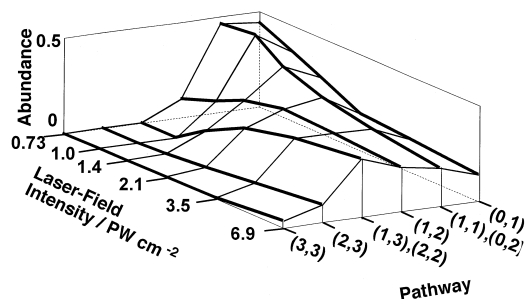


Fig. 7. The three-dimensional presentation of the abundances of the singly and multiply charged parent ions,  $N_2^{p+}$  ( $p=1-6$ ), prior to the fragmentation plotted as a function of the laser-field intensity and the charge number. The relative abundances of the parent ions were calculated from the yields of the corresponding explosion pathways in Table 2.

the (0, 2) and (1, 1) pathways and as the sum of the (1, 3) and (2, 2) pathways, respectively. As the laser-field intensity increases, the yields of the  $N_2^{(p+q)+}$  ions decrease monotonically for  $p + q = 1$  and 2, while those for  $p + q \geq 4$  increase gradually. The intermediate behavior can be seen for  $N_2^{3+}$ , i.e. the yield for  $p + q = 3$  increases in the low laser-field intensity region, and reaches maximum at 2.1 PW/cm<sup>2</sup>, and then decreases in the higher laser-field region. It should be stressed that the procedure to evaluate the relative yields of the Coulomb explosion pathways from the MRMI maps introduced in the present study enabled us to derive the laser-field intensity dependence of the abundances of the singly and multiply charged parent  $N_2^{(p+q)+}$  ions relevant to the fragmentation processes in the intense laser field.

## 6. Summary and conclusions

(1) The high-resolution TOF mass spectra of the  $N^+$ ,  $N^{2+}$ , and  $N^{3+}$  ions produced after the Coulomb explosion were measured at six different laser-field intensities ranging from 0.73 to 6.9 PW/cm<sup>2</sup>. The dependence of the fragment-ion abundances on the laser-field intensity supported the assignments of the Coulomb explosion pathways proposed by the momentum matching of the fragment ions. It has been demonstrated that the high resolving power of the TOF spectrum is powerful to correlate the fragment ions formed after the Coulomb explosion. In total the six explosion pathways, (1, 1), (1, 2), (1, 3), (2, 2), (2, 3), and (3, 3), were identified in addition to the (0, 1) and (0, 2) dissociation pathways.

(2) Imaging techniques have been used to visualize the angular distribution of the photofragments produced after the photodissociation [47–50], and found to be useful to investigate the mechanism of photodissociation processes. Since a number of ion species were ejected from the multiply charged parent ions almost at the same time in the case of the molecular Coulomb explosion, a technique for mass selection should be combined for such an imaging method. In the present study, by rotating a laser polarization angle with respect to the detection axis of the TOF mass spectrometer, the angular and radial momentum distributions of  $N^{q+}$  ( $q = 1-3$ ) fragment

ions were obtained in the form of the MRMI maps. The MRMI map visualizes angular information of a momentum distribution of mass-selected fragment ions on a two-dimensional plane. From the maps, the assignments of the explosion pathways derived from the momentum-scaled TOF spectra were confirmed by comparing the crescent-shaped radial and angular momentum distributions of the fragment ions in the different charge channels.

(3) A method to construct theoretical MRMI maps was introduced, in which a finite ion detector size was taken into account. From the theoretical simulations of the MRMI maps, it has been explained how the dynamical information is encoded in the two-dimensional MRMI map, and the procedure to extract the information about the ultrafast Coulomb explosion processes from the MRMI is discussed. A general procedure was also proposed to evaluate the relative yields of the explosion pathways from the three-dimensional integration of the MRMI maps.

## Acknowledgements

The present work has been supported by the CREST (Core Research for Evolutionary Science and Technology) fund from Japan Science and Technology.

## References

- [1] A. Giusti-Suzor, F.H. Mies, L.F. DiMauro, E. Charron, B. Yang, *J. Phys. B* 27 (1994) 1.
- [2] S. Chelkowski, A. Conjusteau, T. Zuo, A.D. Bandauk, *Phys. Rev. A* 54 (1996) 3235.
- [3] L.J. Frasinski, K. Codling, P.A. Hatherly, *Phys. Rev. Lett.* 58 (1987) 2424.
- [4] L.J. Frasinski, K. Codling, P.A. Hatherly, *Phys. Lett. A* 142 (1989) 499.
- [5] L.J. Frasinski, K. Codling, P.A. Hatherly, *Science* 46 (1989) 1029.
- [6] K. Codling, L.J. Frasinski, P.A. Hatherly, M. Stankiewicz, *Phys. Scr.* 41 (1990) 433.
- [7] P.A. Hatherly, L.J. Frasinski, K. Codling, A.J. Langley, W. Shaikh, *J. Phys. B* 23 (1990) L291.
- [8] M. Brewczyk, L.J. Frasinski, *J. Phys. B* 24 (1991) L307.
- [9] K. Codling, C. Cornaggia, L.J. Frasinski, P.A. Hatherly, J. Morellec, D. Normand, *J. Phys. B* 24 (1991) L593.
- [10] L.J. Frasinski, P.A. Hatherly, K. Codling, *Phys. Lett. A* 156 (1991) 227.

- [11] K. Codling, L.J. Frasinski, *J. Phys. B* 26 (1993) 783.
- [12] M. Stankiewicz, L.J. Frasinski, G.M. Cross, P.A. Hatherly, K. Codling, A.J. Langley, W. Shaikh, *J. Phys. B* 26 (1993) 2619.
- [13] P.A. Hatherly, M. Stankiewicz, K. Codling, L.J. Frasinski, G.M. Cross, *J. Phys. B* 27 (1994) 2993.
- [14] J.H. Posthumus, L.J. Frasinski, A.J. Giles, K. Codling, *J. Phys. B* 28 (1995) L349.
- [15] J.H. Posthumus, A.J. Giles, M.R. Thompson, W. Shaikh, A.J. Langley, L.J. Frasinski, K. Codling, *J. Phys. B* 29 (1996) L525.
- [16] C. Cornaggia, J. Lavancier, D. Normand, J. Morellec, H.X. Liu, *Phys. Rev. A* 42 (1990) 5464.
- [17] C. Cornaggia, J. Lavancier, D. Normand, J. Morellec, P. Agostini, J.P. Chambaret, A. Antonetti, *Phys. Rev. A* 44 (1991) 4499.
- [18] C. Cornaggia, D. Normand, J. Morellec, *J. Phys. B* 25 (1992) L415.
- [19] D. Normand, L.A. Lampre, C. Cornaggia, *J. Phys. B* 25 (1992) L497.
- [20] C. Cornaggia, M. Schmidt, D. Normand, *J. Phys. B* 27 (1994) L123.
- [21] C. Cornaggia, F. Salin, C.L. Blanc, *J. Phys. B* 29 (1996) L749.
- [22] C. Cornaggia, *Phys. Rev. A* 54 (1996) R2555.
- [23] K. Boyer, T.S. Luc, J.C. Solem, C.K. Rhodes, *Phys. Rev. A* 39 (1989) 1186.
- [24] A. Hishikawa, A. Iwamae, K. Hoshina, M. Kono, K. Yamanouchi, *Chem. Phys. Lett.* 282 (1998) 283.
- [25] A. Iwamae, A. Hishikawa, K. Hoshina, M. Kono, K. Yamanouchi (to be submitted).
- [26] A. Hishikawa, A. Iwamae, K. Hoshina, M. Kono, K. Yamanouchi, *Res. Chem. Intermed.*, in press.
- [27] A. Zavriyev, P.H. Bucksbaum, H.G. Muller, D.W. Schumacher, *Phys. Rev. A* 42 (1990) 5500.
- [28] D.T. Strickland, Y. Beaudoin, P. Dietrich, P.B. Corkum, *Phys. Rev. Lett.* 68 (1992) 2755.
- [29] J.H. Sanderson, R.V. Thomas, W.A. Bryan, W.R. Newell, P.F. Taday, A.J. Langley, *J. Phys. B* 30 (1997) 4499.
- [30] K. Vijayalakshimi, V.R. Bhardwaj, D. Mathur, *J. Phys. B* 30 (1997) 4065.
- [31] W.T. Hill III, J. Zhu, D.L. Hatten, Y. Cui, J. Goldhar, S. Yang, *Phys. Rev. Lett.* 69 (1992) 2646.
- [32] T. Seideman, M.Y. Ivanov, P.B. Corkum, *Phys. Rev. Lett.* 75 (1995) 2819.
- [33] M. Ivanov, T. Seideman, P. Corkum, F. Ilkov, P. Dietrich, *Phys. Rev. A* 54 (1996) 1541.
- [34] T. Seideman, M.Y. Ivanov, P.B. Corkum, *Chem. Phys. Lett.* 252 (1996) 181.
- [35] B. Sheehy, B. Walker, L.F. DiMauro, *Phys. Rev. Lett.* 74 (1995) 4799.
- [36] B. Sheehy, L.F. DiMauro, *Annu. Rev. Phys. Chem.* 47 (1996) 463.
- [37] T. Seideman, *J. Chem. Phys.* 106 (1997) 2881.
- [38] H. Stepelfeldt, H. Sakai, E. Constant, P.B. Corkum, *Phys. Rev. Lett.* 79 (1997) 2787.
- [39] Z. Vager, R. Naaman, E.P. Kanter, *Science* 244 (1989) 426.
- [40] N. Saito, H.I. Suzuki, *Phys. Rev. Lett.* 61 (1988) 2740.
- [41] S. Hsieh, H.D. Eland, *Rapid Commun. Mass Spectrom.* 9 (1995) 1261.
- [42] M. Lundqvist, D. Edvardsson, P. Baltzer, B. Wannberg, *J. Phys. B* 29 (1996) 1489.
- [43] P.A. Hagan, J.H. Eland, *Rapid Commun. Mass Spectrom.* 3 (1989) 186.
- [44] S.L. Varghese, C.L. Coke, E.Y. Kamber, V. Frohne, *Nucl. Instrum. Methods, Phys. Res. B* 40 (1988) 266.
- [45] H. Tawara, T. Tonuma, H. Kumagai, T. Matsuo, *J. Phys. B* 25 (1992) L423.
- [46] J. Ullrich, R. Moshhammer, R. Dorner, O. Jagutzki, V. Mergel, H. Schmidt-Bocking, L. Spielberg, *J. Phys. B* 30 (1997) 2917.
- [47] P.W. Chandler, P.L. Houston, *J. Chem. Phys.* 87 (1987) 1445.
- [48] T. Kinugawa, T. Arikawa, *J. Chem. Phys.* 96 (1992) 4801.
- [49] T. Suzuki, K. Tonokura, L.S. Bontuyan, N. Hashimoto, *J. Phys. Chem.* 98 (1994) 13447.
- [50] Y. Sato, Y. Matsumi, M. Kawasaki, K. Tsukiyama, R. Bersohn, *J. Phys. Chem.* 99 (1995) 16307.